ELECTROCHEMICAL NANOGENERATORS FOR WEARABLE ENERGY HARVESTING

By

Murtaza Zohair

Thesis

Submitted to the Faculty of the

Graduate School of Vanderbilt University

in partial fulfillment of the requirements

for the degree of

MASTER OF SCIENCE

in

Interdisciplinary Materials Science

May 31, 2020

Nashville, Tennessee

Approved:

Cary L. Pint, Ph.D.

Piran R. Kidambi, Ph.D.

ACKNOWLEDGMENTS

TABLE OF CONTENTS

LIST OF FIGURES

LIST OF TABLES

LIST OF PUBLICATIONS

1. Zohair, M. *et al.* Continuous Energy Harvesting and Motion Sensing from Flexible Electrochemical Nanogenerators: Toward Smart and Multifunctional Textiles. *ACS Nano* **14**, 2308–2315 (2020).

CHAPTER 1

INTRODUCTION

1.1 Motivation

The energy needs for the next stage in technological development demand miniaturization and redesign of energy sources to meet the progress of electronics. Dispersed networks of devices in applications like point of care diagnostics and wearable electronics require reliable local energy sources that can be incorporated without compromising form, function, or safety. This challenge has promoted two congruent research efforts in the areas of high energy density batteries and ambient energy harvesting.

1.2 Ambient Mechanical Energy Harvesting

There are several renewable and ambient energy sources available for conversion to electrical energy which can largely be broken down into classes of mechanical, thermal, and radiant. A familiar example is the use of a wind turbine to utilize the mechanical energy from wind to drive a generator. Table 1 shows examples of various ambient energy sources and their power densities. Clearly, the choice of ambient source is highly dependent on the application it is used for. To drive low power electronics can range from microwatts to a few miliwatts. Solar panels are a pervasive energy harvesting technology; their high areal power densities and lack of moving parts make them ideal for roof fixtures but the reduced power indoors, fragile and expensive materials, and limited harvesting time make them ill fitted for the small devices discussed above.

Among these sources, mechanical energy is the most readily available ambient energy source for mobile applications, especially for on the body applications. Mechanical energy from the body is obtained either through the kinetic energy from the movement of a rigid body, i.e. the swinging of a leg, and through elastic deformation such as the expansion of the heart during beating.[1]

Ambient Energy Source	Power Density
Acoustic Noise[2]	$0.003\ \mu W/cm^3$ @ 75Db $0.96\ \mu W/cm^3$ @ 100Db
Ambient Radio Frequency[3]	$1\ \mu W/cm^3$
Solar	$100\ mW/cm^2$ (direct sunlight) $100\ mW/cm^2$ (illuminated office)
Airflow[4]	$1\ \mu W/cm^2$
Heel Strike[5]	$7\ W/cm^2$
Blood Pressure[6]	0.93 W at 100 mmHg

Table 1: Examples of ambient energy sources adapted from Tan (2010) and Yildiz (2009).[7,8]

The method used to convert mechanical energy to electricity can significantly reduce the power density of the harvested energy depending on the conditions of movement. Most energy harvesting devices rely on converting the vibrational energy from human motion to an alternating current, with the current being a function of both the amplitude and frequency of the movement. Human motion, however, mostly lies below 5 Hz and is nonuniform, which represents non-ideal conditions for many of these devices. Triboelectric generators (TEG) rely on the large charges accumulated on dielectric surfaces during contact and have the advantage of high voltages, however, reliance on contact-separation or sliding modes can lead to bulky systems not compatible with building block integration into textiles or wearables.[9–13] Similarly electromagnetic generators require rotating or sliding parts, which has made them difficult to manufacture and miniaturize.[14–

[16] Piezoelectric generator (PEG) fibers can have compact forms when using polyvinylidene difluoride (PVDF) fibers and their composites, however these devices are limited to inefficient operation and low power outputs in the frequency range of human motion.[17–19] Most promising so far is the Twistron energy harvester, which leverages the change in the double layer capacitance due to a change in the exposed surface area for power generation,[20] though decreased performance at neutral pH and limitations of charge storage availability in a capacitive material provide ongoing routes for this design and integration.

1.3 Electrochemical-Mechanical Coupling

Electrochemical generators (ECG) are a new class of energy harvesting device that are based on stress-induced potential gradients that result in ion diffusion and electrical current generation, and are better synced to the timescale of human motion compared to alternative approaches.[21–24] The principle behind this phenomenon has been used to describe a crystalline solid with a diffusional species, such as in the treatment of ions in silicate glasses or interstitial species in metal electrodes.[25] In this treatment, the chemical potential of the diffusive species, I, is dependent on both the composition of the system and the elastic stresses. Starting from the differential of the Helmholtz free energy (F):

$$dF = \sigma_{ij}d\varepsilon_{ij} - SdT + \rho_0\sum(\mu_I dc_I) \qquad \text{(Eq 1)}$$

Where σ_{ij} is the stress tensor, ε_{ij} is the strain tensor, S is the entropy, T is the temperature, ρ_0 is the molar density, μ_I is the chemical potential of species I, and c_I is the concentration of species I. We can derive the relation between chemical potential, stress, and strain for a binary solution which gives the following equation:

$$\mu_I(\sigma_{ij}, c) = \mu_I^0 + RTln(a_I) - V_0\left(\frac{d\varepsilon_{ij}}{dc}\right)\sigma_{ij} - \frac{1}{2}V_0\left(\frac{dS_{ijkl}}{dc}\right)\sigma_{ij}\sigma_{kl} - V_0\left(\frac{d\varepsilon_{kk}}{dc}\right)P +$$

$$\frac{1}{2}V_0\left(\frac{dS_{jjkk}}{dc}\right)P^2$$

(Eq 2)

Where a_I is the activity of species I, V_0 is the molar volume, P is the pressure, and S is the compliance matrix. These equations are simplified for homogenous, isotropic systems where the elastic terms do not change with concentration, which will be an approximation applied in later chapters. From equation 2 we see that stress gradients in this system lead to chemical potential gradients. This drives diffusional flux of the mobile species along the chemical potential gradient.
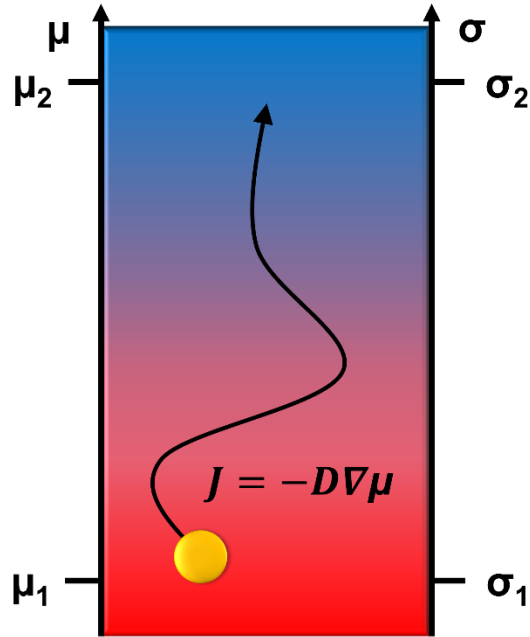
Figure 1: Simplified diagram for the model of a stress field in a lattice that creates a chemical potential gradient and drives the diffusional movement of a mobile species.

The stress component of the chemical potential has found relevance in electrochemical systems such as batteries and supercapacitors due to their impact on the solid components of these devices, contributing the growth of dendrites, reduction of ion conductivity, and pulverization of silicon among other important challenges in this field.[26–30] The effect has also been leveraged to

modify reaction potentials, increase ion diffusivity, and harvest mechanical energy.[21,22,24,31–33] ECGs have only until now been constructed in planar electrode geometries, however, in contrast to existing platforms for energy harvesting, a variety of materials can be integrated into ECG devices, such as biocompatible materials that can facilitate the design of multifunctional textiles.[34]

1.4 Wearable Energy Devices

Some constraints for energy generation from the body comes from the ability of these devices to be embedded in packaging that does not encumber natural motion, pose a safety concern, or compromise comfort. This has led to the development of textile and fiber-based energy devices. From wearable biomedical devices, sweat or biochemical sensors, electronics, and other wearable systems – better technology functionality is being designed into systems, often utilizing nanoscale design approaches.[35–43] Design approaches for wearable electrochemical energy devices are similar to those used for any multifunctional energy platform with electrodes, active material, and electrolytes that withstand the mechanical stresses incurred during movement and bending. Many of these devices use carbon, especially nanocarbons like carbon nanotubes (CNT) and graphene as flexible current collectors.[44,45] Another through line is the use of solid polymer and gel polymer electrolytes as a safer and more stable alternative to traditional liquid organic electrolytes. The most important consideration is the stresses incurred at the interface, which is often the site of initial mechanical failure. We have drawn on our previous work in structural batteries and supercapacitors in designing a fiber-based electrochemical energy device.[46–48]

The fiber-based approach has the advantages of being easily incorporated into existing textile manufacturing infrastructure, where these fibers can be substituted for the traditional spool of yarn.[49–53] The common construction technique involves coating traditional textile fibers with

conductive additives and electroactive material. The coatings can be applied by slurry casting as in traditional electrode lay-up or by functionalizing the surface of the fibers. Jost and colleagues, for example, demonstrated the use of inexpensive materials like natural cotton fibers which were infiltrated with ionic liquid to create a conductive composite with steel yarns. Techniques involving chemical baths such as electroless, electrophoretic, and electrochemical deposition are attractive because they bypass the additional weight of binders and can be done quickly.

In this study, we characterize an energy harvesting yarn comprised of biocompatible Prussian blue nanoparticles that exhibits dual function for either human motion energy harvesting and/or continuous sensing of biomechanical motion.

CHAPTER 2

METHODS

2.1 KPB deposition on CNT/Polyester Fibers

Iron (III) Chloride ($FeCl_3 \cdot 6H_2O$, 98%) was purchased from Honeywell, and Potassium Ferricyanide ($K_3Fe(CN)_6$, 99%) and Potassium Chloride (KCl, 99%) were purchased from Alfa Aesar. The CNT/polyester fibers (Electro-Yarn) were cut into segments (5 cm when sealed in Kapton tape and 9 cm for sewing into textiles) and taped to a copper foil tab. The cathodic galvanostatic deposition is adapted from the method previously described by Itaya *et al.*[54] The fibers were submerged in a bath containing 0.025 M Hydrochloric Acid (HCl), 0.1 M KCl, 0.01 M $K_3Fe(CN)_6$, and 0.01 M $FeCl_3 \cdot 6H_2O$ in a 40 mL aqueous bath. A platinum wire is used as a counter electrode. The deposition is run at a constant current of 15 $\mu A/cm^2$ for 25 minutes using an Autolab PGSTAT 101. After the deposition process the fibers were thoroughly washed with deionized water and dried under ambient conditions.

2.2 PVA Gel Electrolyte Synthesis

The PVA gel electrolyte was prepared by mixing 2 g of PVA and 3 g of KCl in 20 mL of water at 90°C for several hours until dissolved. The fibers were overcoated with the solution and allowed to dry overnight under ambient conditions.

2.3 KPB Characterization

The morphology and composition of the deposited film is characterized using a Zeiss Merlin scanning electron microscopy (SEM) for SEM and EDS measurements. Cyclic Voltammetry (CV) measurements are done using an Autolab PGSTAT 101 at room temperature with a voltage range of -0.2 to 1.1 V at a constant scan rate of 20 mV/s. The measurements were performed in an aqueous solution of 1 M KCl with a platinum foil counter electrode and a KCl saturated calomel reference electrode. Raman measurements were performed using a Thermo Scientific DXR Raman microscope with 532 nm laser excitations.

2.4 ECG Assembly and Testing

3-5 fibers are put on either side of GE Whatman glass microfiber separator soaked with an aqueous solution of 1M KCl in DI water and encased in polyimide tape. To measure changes in the potential from ion size measurements, 1M NaCl or 1M LiCl in DI water were used as the electrolyte. The fibers on either side act as opposite electrodes, and a copper tab is used as an electrical contact to the uncoated end of the CNT yarn electrodes. A programmable Arduino set with a Servo motor performs controlled bending and unbending cycles around cylinders of varying diameters. During cycling, open circuit voltage (OCV) and short circuit current (SCC) are measured using an Autolab PGSTAT 101 system to find the peak power output of the device during bending. The SCC is represented as a current density normalized by the active area under bending stress, which is estimated by taking the arc length of the radius of curvature (cylinder radius) at a bending angle of 90° and bending radius of 8 mm. The devices are connected in short circuit mode for 2 hours prior to testing to reduce the inhomogeneity between electrodes that

causes background current and voltage. The fibers are integrated into textiles as by sewing 9 cm long fibers into 2 fabrics that are sandwiched with a 1M KCl/polyvinyl-alcohol (PVA) gel electrolyte and fiberglass separator to ensure shorting does not occur.

CHAPTER 3

RESULTS AND DISCUSSION

Here we design an aqueous-based platform utilizing biocompatible active materials and set into a 3-D geometry of a fiber or yarn to enable integration into fabrics and textiles. To accomplish this, we chose Potassium Iron Hexacyanoferrate, more commonly known as Prussian blue (PB), as an active material for our devices. Notably, PB has a long history of biocompatible applications including being used as the blue powder for fingerprinting, and its unique open-framework structure and electrochemical stability have prompted numerous studies on the use of PB and its analogues in battery electrodes, biosensors, and electrochromic devices.[34,55,56] PB has an open-framework hexacyanometalate crystal structure with the chemical formula $A_x Fe(II)[Fe(III)(CN)_6]_{1-y} \cdot z H_2 O$, where A is an alkali ion that can reversibly be inserted into the interstitial sites of the framework. The large interstitial channels aid in fast kinetics of insertion for large ions and molecules, like potassium, to provide the central chemical functionality of a flexible electrochemical nanogenerator during human motion. To couple this into a fiber, we utilize an aqueous based chemistry with the PB and conductive current collector fibers designed from CNT/polyester fibers as is demonstrated in **Figure 2a**. In this design, CNT coated polyester fibers are a transferrable platform that is simply conductive, lightweight, and non-corrosive in the operating condition of the generator. PB was electrochemically deposited on the CNT yarns using a cathodic galvanostatic deposition process in an aqueous precursor solution of potassium ferricyanide and iron (III) chloride, which produced nanoscale networks of PB.[54] This electrochemical deposition method requires direct charge transfer between the deposited material

(PB) and the surface upon which it is deposited (CNTs) that is known to facilitate better mechanical interface adhesion than other deposition techniques. Additionally, the CNTs that are being used in our work possess a high content of sp^3 hybridized carbons (**Figure 7**), which also facilitates strong and covalent out-of-plane adhesion across the carbon-PB interface, combined with favorable π-stacking and ionic interactions.[57] Together, this enables a stable interface design that we attribute to observed mechanical stability of flexible PB/CNT fibers during handling and testing in this work. **Figure 2b** shows the electrochemical deposition curve, which results in a film thickness nearing 1 μm after 25 min. This one-step coating technique was chosen due to the ability to achieve high throughput and scale this design to practical levels for textile manufacturing.
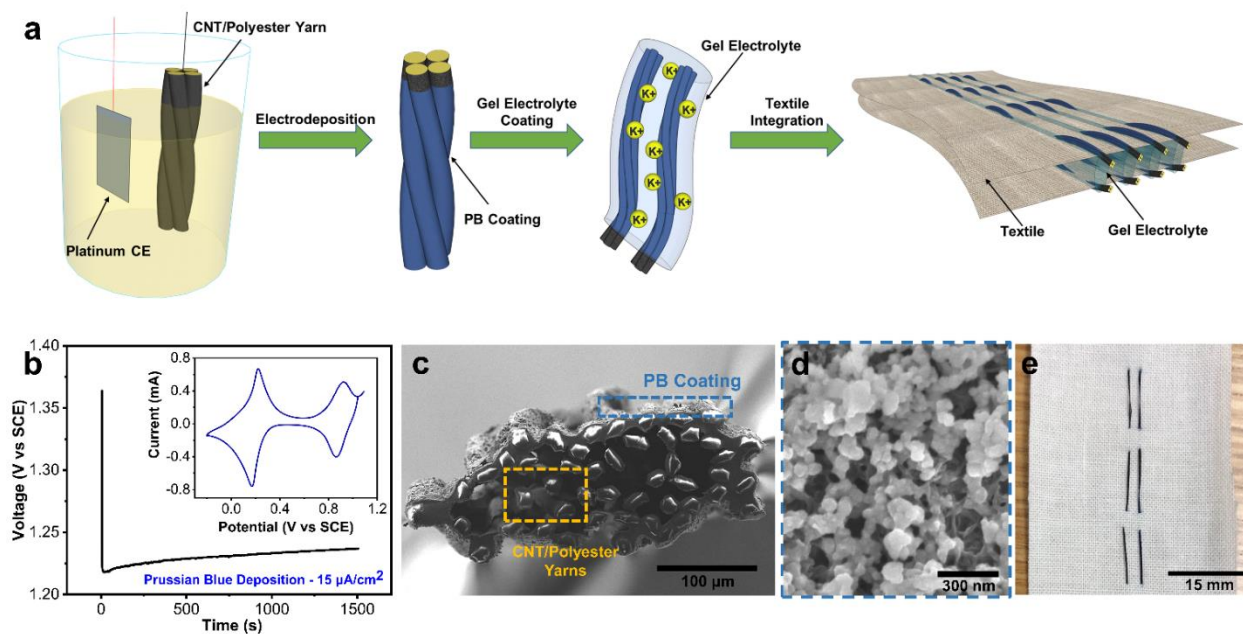
Figure 2: (a) schematic of ECG yarn fabrication. (b) cathodic electrochemical deposition of PB and inset graph of characteristic CV peaks. (c) SEM images of KPB coated CNT/polyester yarn cross-section and (d) KPB coating microstructure. (e) picture of 2 ECG yarns stitched into a cotton cloth.

To characterize the coated PB materials, we carried out cyclic voltammetry (CV) measurements to confirm reversible redox reactions associated with potassium insertion and extraction into the PB framework, as shown inset into **Figure 2b**. The peaks at 0.2 and 0.9 V corresponding to the reduction to Prussian White (PW) and oxidation to Berlin Green (BG) respectively demonstrate the characteristic behavior of electrochemically active PB.[54] Raman and energy-dispersive X-ray spectroscopy (EDS) also were used to confirm the formation of PB, with full spectra provided in supporting information **Figures 3 and 4.**[58]
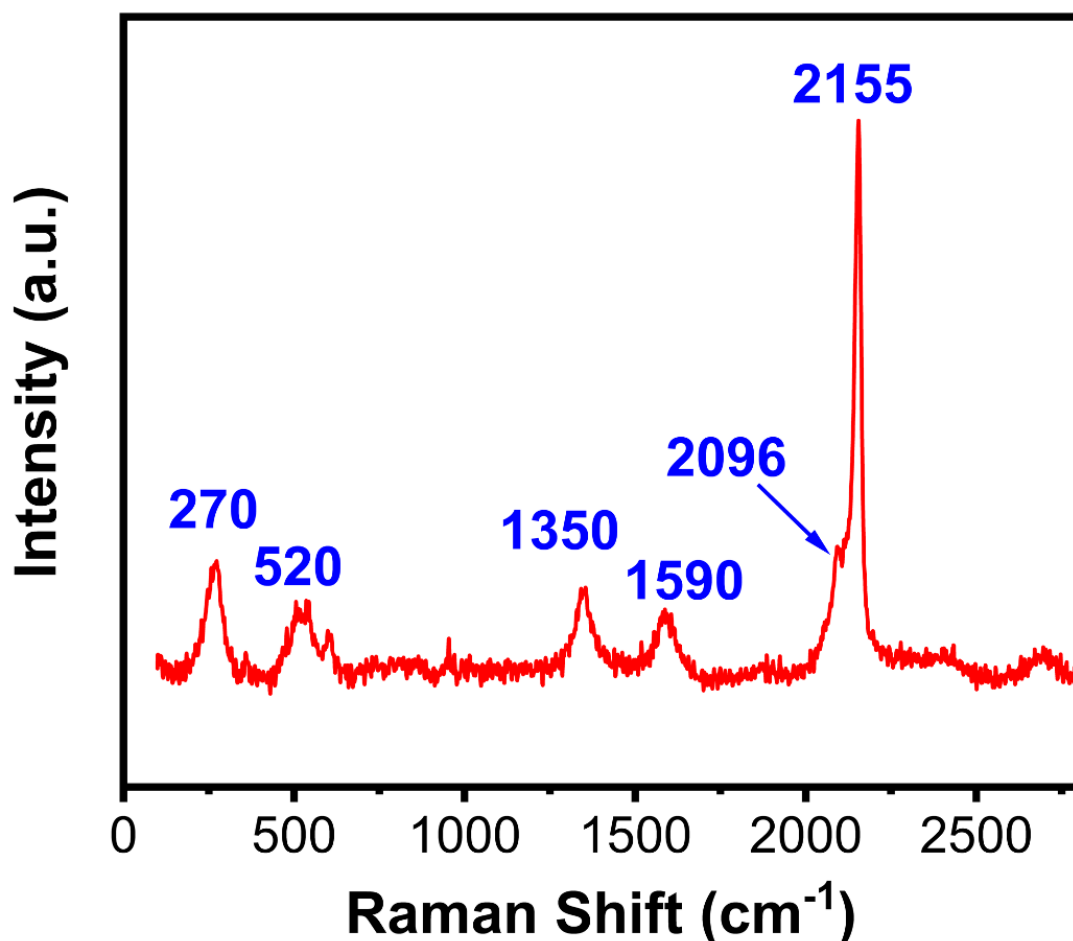
Figure 3: Raman spectrum of PB coated CNT Fibers. Note that peaks labeled at 1350 cm^{-1} and 1590 cm^{-1} represent the D and G bands of the CNTs that correlate to the sp^3 and sp^2 hybridized carbon species in the CNTs. In this case, a significant amount of sp3 hybridized carbon is expected to, along with the galvanostatic electrodeposition of PB, promote uniform and robust interfaces needed for handing and testing flexible fibers and devices.
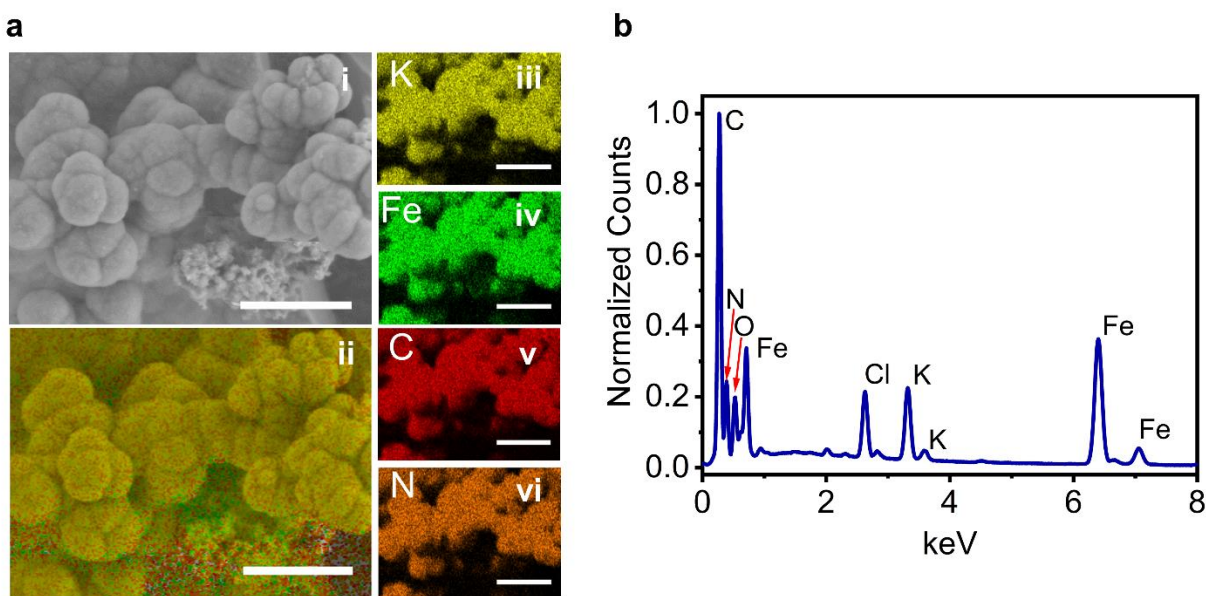
Figure 4: EDS spectrum and images of PB nanoparticles deposited on CNT fibers, scale bar = 2 μm.

Figure 2c shows a cross sectional view of the electrodeposited PB coating on the CNT fiber, which radially covers the outside of the CNT/polyester fiber bundle due to the uniform electric field that guides electrodeposition. Top-down SEM images further demonstrate a porous network of spherical particles in **Figure 2d**. The assembly of the energy-harvesting system emulates a battery device, but with a symmetric electrode configuration. To accomplish this, we combined two coated PB/CNT fibers together with a PVA-KCl matrix to produce the resulting energy harvesting fiber. Whereas details of the fiber performance will be subsequently discussed at length, **Figure 2e** shows the harvester stitched into a cotton fabric as a textile integrated energy harvester highlighting the desired function for our study.

To design a flexible ECG with maximum power output, our materials selection approach was agnostic of the ion species since PB is an open framework structure compatible with Li, Na, and K ions, and each of these species may exhibit different mechano-chemical response.

Therefore, to study these key design parameters, we prepared devices incorporating fiber-based electrodes tested in liquid electrolytes so that that the optimized performance could be evaluated independently from variables associated with solid fiber preparation. Generally, in an ECG device, two symmetric fibers are connected *via* an electrolyte and, when bent, generate power based on the coupling between the electrochemical potential of the material and the mechanical state of the active material. By bending a fiber in this configuration, a chemical potential difference is generated between the compressed (higher potential) material and the tensed (lower potential) material, causing the flow of ions between the two electrodes (*e.g.* the two fibers wrapped together in a yarn). The chemical potential difference and electrical current generated due to bending are measured using open circuit voltage (OCV) and short circuit current (SCC) measurements and together constitute the power and energy output of the device. Therefore, our first aim was to study the role of different ion species including Li, Na, and K on the mechanical-chemical coupling in the harvester, and hence the total power and energy output by varying the electrolyte solution from KCl to LiCl and NaCl. Experiments conducted to assess the OCV of similarly prepared PB electrodes in an ECG device indicate that the OCV response of KPB is between 4-5 times greater than that of LiPB and the highest of all three cation species studied, as shown in **Figure 5**.
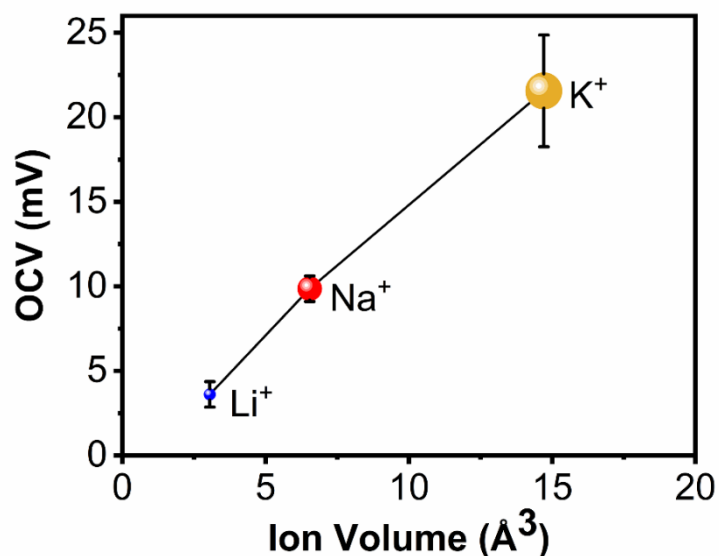
Figure 5: Peak voltage (OCV) of harvesters during 8 mm bending experiments at 0.1 Hz based on the mechanistic insertion/extraction of Li^+, Na^+, or K^+ through variation of electrolyte media.
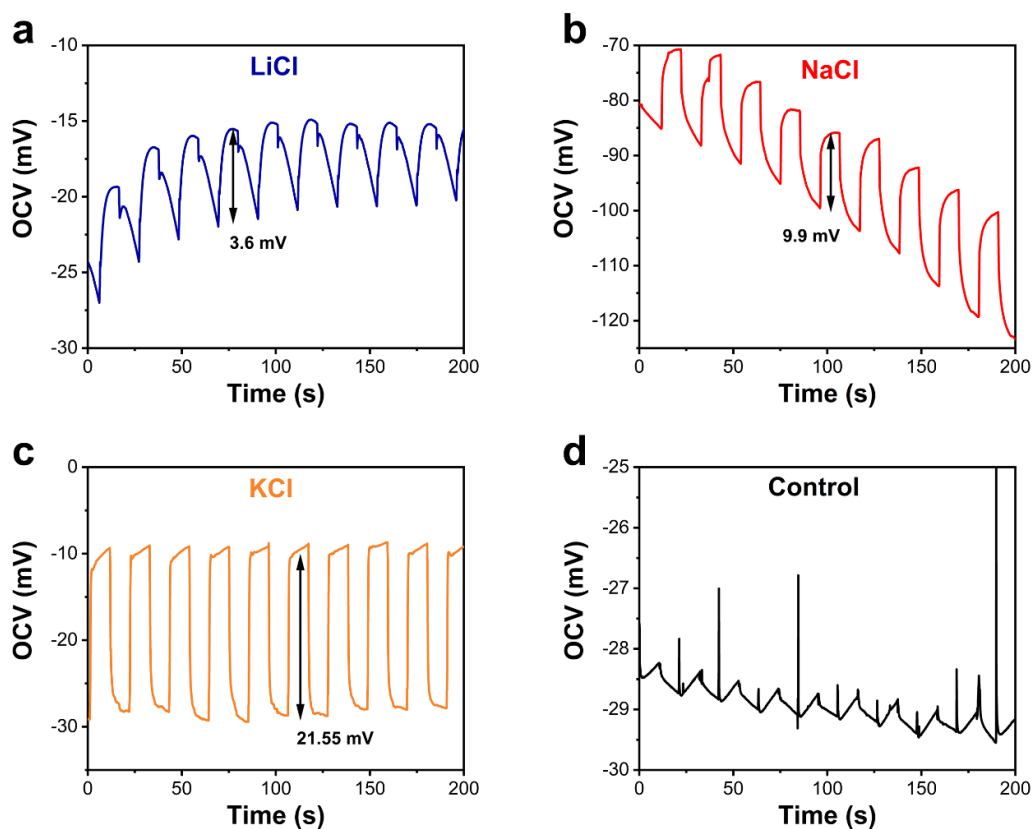
Figure 6: OCV measurements during bending tests with 8 mm bending radii of the PB ECG in electrolytes containing (a) 1M LiCl (b) 1M NaCl (c) 1M KCl and (d) a control harvester with no salt added to the deionized water.

15

To understand this result, we can utilize solution thermodynamics to express the relation between the equilibrium chemical potential (μ_k) and an applied stress as:

$$\Delta\mu_k = \Delta\phi = \Omega\sigma_H \qquad (1)$$

where $\Delta\phi$ is the voltage difference across the electrodes and σ_H is the hydrostatic stress. In **eq 1**, stress is scaled by a coupling parameter, Ω, which is equal to the partial molar volume, or $\partial V/\partial n$, describing the change in volume (V) associated with the insertion of a charged species (n).[28] At the molecular level, bending the device creates a chemical potential gradient between the electrodes that drives the flow of cations from occupied sites on the compressed side (high chemical potential) into vacant and large interstitial sites of the face centered cubic PB lattice of the tensed electrode (low chemical potential). This is facilitated by the interstitial insertion/extraction mechanism for alkali ions in PB that enables reversible stress-driven ion flow. In turn, the resulting chemical potential difference per unit charge will be dependent upon the total size of the ion, and maximized when using the largest ion species, which in our case is K. As a result, since only Na and Li have been studied for mechanical-electrochemical coupling relevant to ECG operation in the literature so far, our results highlight K as a superior cation species for this purpose. With this said, whereas K is less advantageous to a battery electrode than Li due to larger volume per charge, and less electronegativity, K is in fact more advantageous to an ECG device than Li due to the greater chemical potential per unit charge produced during insertion/extraction. Further experiments conducted leverage the use of KPB rather than either LiPB or NaPB for this reason.
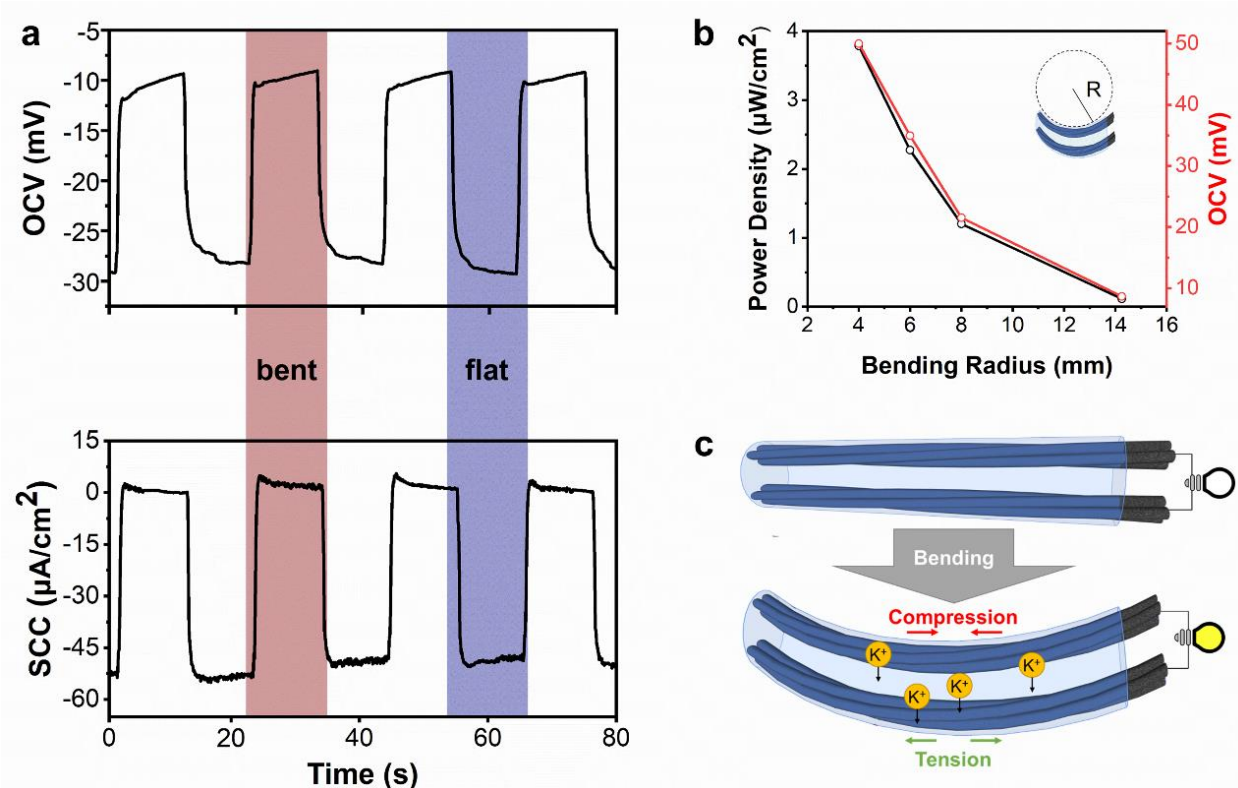
Figure 7: (a) SCC and OCV response during controlled bending cycles at 0.1 Hz and 8 mm bending radius in liquid electrolyte. (b) Inverse relationship of power output and OCV with bending radius. (c) Schematic representation of the working principle of energy harvesting in ECG fibers.

To demonstrate the operation of the KPB harvester, we performed repeated bending and unbending cycles for a typical PB device in a liquid electrolyte solution of 1M KCl as shown in **Figure 7a** at a bending rate of 0.1 Hz. The current spikes at the onset of bending due to the movement of K ions associated with the input stress, continues and slowly decays when held as the insertion/desertion of K ions relieves the applied external stress on the electrodes. Upon returning to the flat state, the concentration gradient that resulted from stress-driven ion flow causes a reverse current to re-establish the equilibrium ion concentration. At an 8 mm bending radius the measured peak SCC response is ~55 $\mu A/cm^2$ and peak OCV response is ~23 mV, which are significantly higher in comparison to lithium silicon (2.5 mV) and sodium-phosphorene (5 mV)

harvesters which utilize Na and Li alkali ions, respectively.[21,24] Further, integrating the SCC over the 10 second bending period gives the charge of migrated K ions as ~ 123.5 μC. Comparing this to the specific capacity of PB of 170 mAh/g (or 612 C/g), a full charge-discharge cycle with a control mass ~ 58 μg produces total charge ~ 35.6 mC, which correlates to ~ 6% total volume expansion of the PB. Assuming uniform charge occupation in the PB, the average volume expansion of the PB during a typical bend-unbend cycle is then estimated from our measurements as ~ 0.02%, which is a few orders of magnitude lower than commonly used Li battery electrode materials. Not only does this make interface delamination due to shear stresses during bending-induced charge insertion/extraction negligible relative to that observed for battery interfaces, but it highlights an important design criteria between batteries and ECGs. A good ECG is a device that uses a very small amount of charge relative to the total available capacity on any one bend/unbend cycle whereas a good battery is a device that uses all available storage capacity on every cycle. In turn, whereas K-ion battery electrodes can be challenging to design given the expectation of plastic deformation or cracking during deep charge/discharge processes[59], ECG devices exhibit a shallow charge depletion that makes such effects negligible during operation.

Along with the coupling parameter, the stress can also be modulated by decreasing the bending radius as shown in **Figure 7b**. Here, the minimum bending radius was chosen to be 4 mm due to this representing the smallest radius of movable joints in the human body in the fingers, where the bending radius at the head of the joint at 90° can be approximated as 4 mm. Notably, it is common in literature to evaluate generators with lower bending radii and often in folding tests to achieve higher and/or maximum reported current response, even though these tests are less useful toward evaluating human motion energy harvesting capability. At a 4 mm bending radius, which is a small bending radius relative to human motions, the product of the OCV and SCC yields

a peak power of 3.8 µW/cm² at 0.1 Hz. By calculating the hydrostatic stress on the electrode during bending at various bending radii, the experimental voltage to stress coupling parameter is calculated to be 36 mV/GPa for KPB. The equations and values used to calculate this can be found in **Figure 8**. Data from the lattice expansion of PB during sodiation gives an approximate 5% increase in the volume of the unit cell when Na ions occupy the 4 interstitial sites in the lattice.[60–62] The approximate partial molar volume based on the observed volume change is 7.5 cm³/mol, which corresponds to a theoretical coupling parameter of 78 mV/GPa for Na ion insertion in PB. With K ion insertion, the theoretical coupling parameter is expected be even larger due to greater volume expansion. The reduced coupling parameter is likely due to relaxation-induced losses at nanoparticle interfaces that reduce stress transfer.

$$\sigma_H = \sigma_{xx} + \sigma_{yy}$$
$$\sigma_{xx} = h\frac{E}{(1-v^2)R}$$
$$\sigma_{yy} = h\frac{vE}{(1-v^2)R}$$

$\Delta\phi = \Omega\sigma_H$

Parameter	Value
Young's Modulus (*E*)	21.3 GPa
Poisson Ratio (*v*)	0.352
Height (*h*)	0.3899 mm
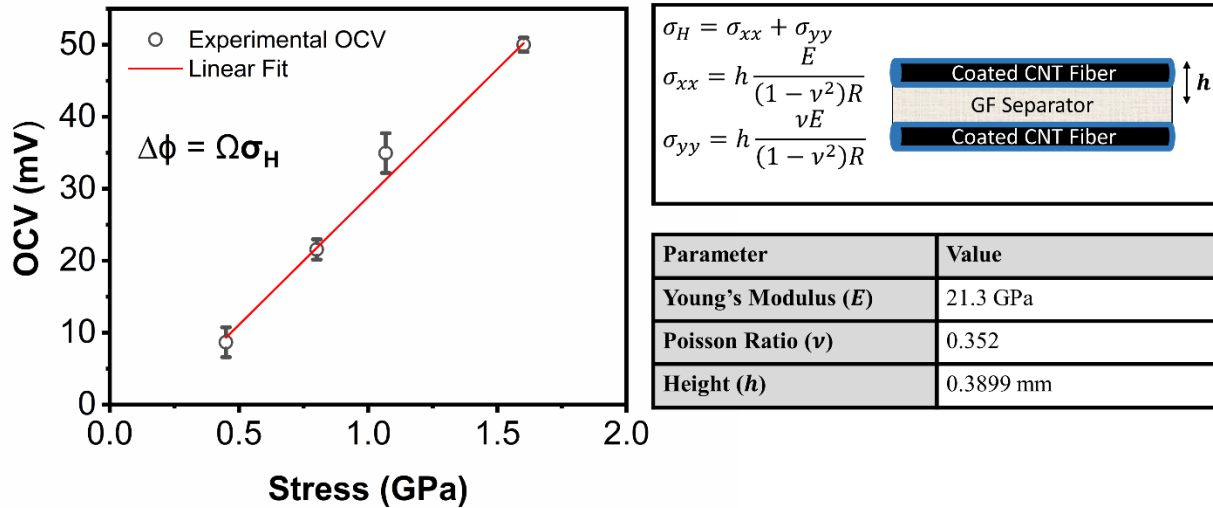
Figure 8: Linear relationship between OCV and stress calculated from bending radii of the PB ECG in 1M KCl at a 0.1 Hz bending frequency. Values for Young's modulus and Poisson's ratio are obtained from literature.[66]

Extending these tests to fibers which can be integrated into textiles, a 1M KCl/PVA polymer gel electrolyte is over-coated on two symmetric PB electrodes that are then sewn into fabrics (**Figure 9**). To study the ability to couple the harvester response into a textile, the PVA-

electrolyte harvester stitched into a fabric is compared to a Kapton tape encased harvester with liquid electrolyte in **Figure 9a** and shows nearly identical performance under the same controlled bending conditions. Notably, the noisier signal of the stitched harvester during motion is due to the microscale slippage of fibers in the fabric architecture. Unlike tests conducted under fixed conditions, such as bending radius and bending rate, human motions are more variable and occur over a range of frequencies and bending radii. By extrapolating performance measured over fixed bending radii, we can assess that until a bending radius as large as ~ 33 mm, the measured signal from these harvesters are measurable against background noise (supporting information). Comparing this upper bound of bending radii to the radius of the glenohumeral head (shoulder) ~ 25 mm and femoral condyle (knee) of ~ 22 mm, it can be expected that the primary joint-related bending motions in the human body will lead to a resulting (measurable) electrical/energy harvesting response from these fibers.[63,64] To demonstrate this point, **Figure 9b** demonstrates a harvester acting as a self-powered motion sensor when sewn into the elbow of an arm-sleeve. In this configuration, the current generated by the harvester scales with the bending angle at the elbow as the elbow is moved back and forth from its original position to a bent state. Holding the elbow in a static position for 10 seconds results in the decay of the signal as seen in the 0.1 Hz SCC bending tests of **Figure 7b**. This demonstration highlights the potential for sensing the movement and instantaneous position of body parts during movement, which distinguishes it from other forms of self-powered strain sensors.[9,13,65] Here the change in SCC from the onset of each test is plotted to demonstrate the difference in peak current response over various bending angles. To demonstrate this idea in a different wearable platform, a harvester sewn into the finger of a glove is shown in **Figure 9c**, where the current is generated by bending the finger every 10 seconds. Whereas all tests in our study are performed at room temperature (~ 23°C), low-temperature tests

performed at 5°C (**Figure 10**) that simulate common cold-weather conditions indicate consistent response and sensitivity of the harvester, but with decreased current response attributed to the temperature dependence of the electrolyte ionic resistance. This further embodies the capability to sense the motion and position state of a finger while the finger is being moved, enabling the simultaneous capability of motion sensing and energy harvesting. It also should be noted that whereas future efforts will be required to overcome some variability from the lack of form fitting materials and packaging with textiles to ensure no slippage of the fibers, this result demonstrates the proof of concept for the proposed application. Additionally, it should also be noted that deflection during pressing has been previously shown to generate similar current responses in ECG devices and can be treated as minor bending of the electrodes.[21] This can be used to incorporate self-powered tactile sensors on fingers for applications in human-machine interfaces such as stitched keyboards and remote controllers.
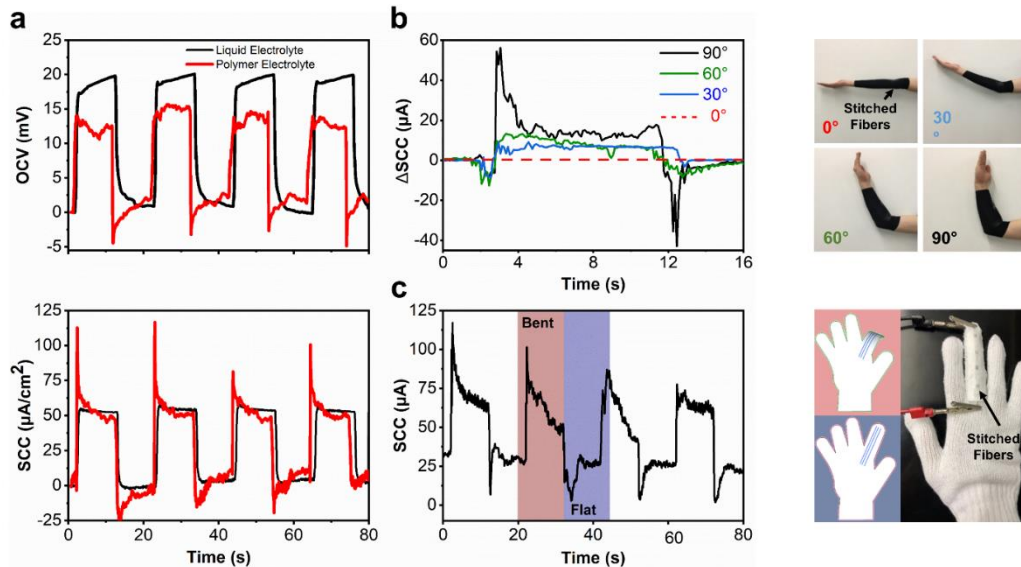

Figure 9: (a) OCV and SCC measurements of ECG yarns with polymer electrolytes (textile) and liquid electrolytes (control) at an 8 mm bending radius and 0.1 Hz bending frequency. (b) SCC response of an ECG stitched into an arm sleeve demonstrating the ability to sense elbow position by bending angle. (c) SCC response during finger bending of an ECG sewn into a glove.
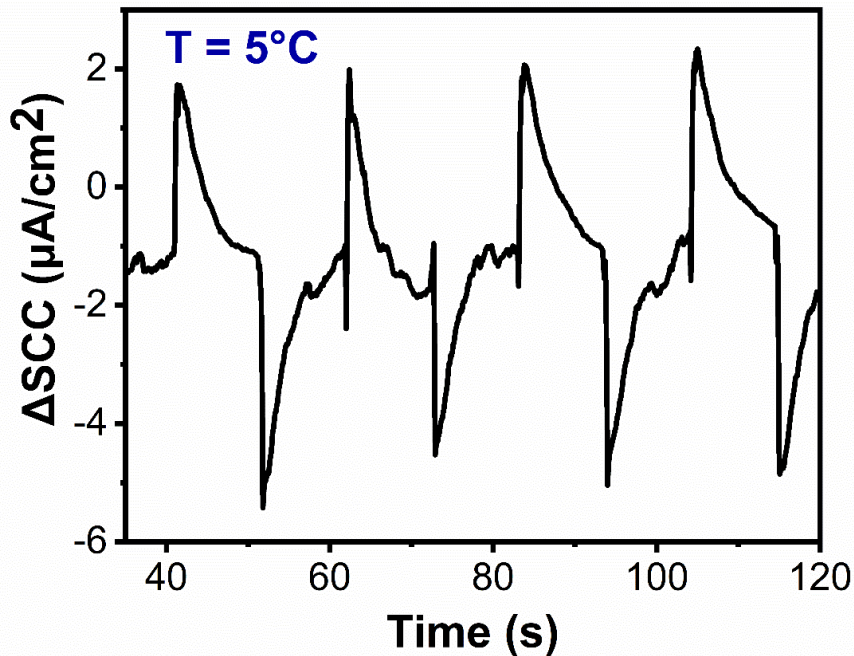
Figure 10: SCC measurements of the PB ECG in 1M KCl with an 8 mm bending radius in a temperature controlled environment at 5°C. Notably, even though the responsivity of the device appears invariant, the current density response is lower than bending tests done at room temperature. This is attributed to the known temperature dependence of electrolytes where the ionic resistance is strongly dependent upon temperature.

To demonstrate the broad performance of our flexible ECG devices against other state-of-the art techniques capable of converting mechanical motion into electrical response, we plotted the comparison of the results from our study to other harvesters that are wearable and exhibit performance within the frequency range of human motion (**Figure 12**). Owing to the kinetics of charge transfer in electrochemical media, our ECG fiber device exhibits a significant peak power output over the target frequency range of human motion that generally spans from 0.1 – 10 Hz that breaks the trend from past work where peak power is compromised under low frequency operation. Compared to triboelectric nanogenerators (TEG), our fibers can exhibit comparable or higher peak power output without specialized design criteria to harness the triboelectric mechanism for power production in a wearable device. Whereas piezoelectric generators (PEG) are better suited than

TEGs for fiber design, the limited number of PEG active materials and a mechanism better suited for higher frequency power harvesting makes it challenging for both peak power and continuous response in the frequency range of human motion. Further, compared to Twistron fibers which are analogous to ECG devices in the way supercapacitors are related to batteries, the slower kinetics and higher charge density of PB battery materials facilitates ECG performance that can more straightforwardly scale continuous operation at low frequencies.
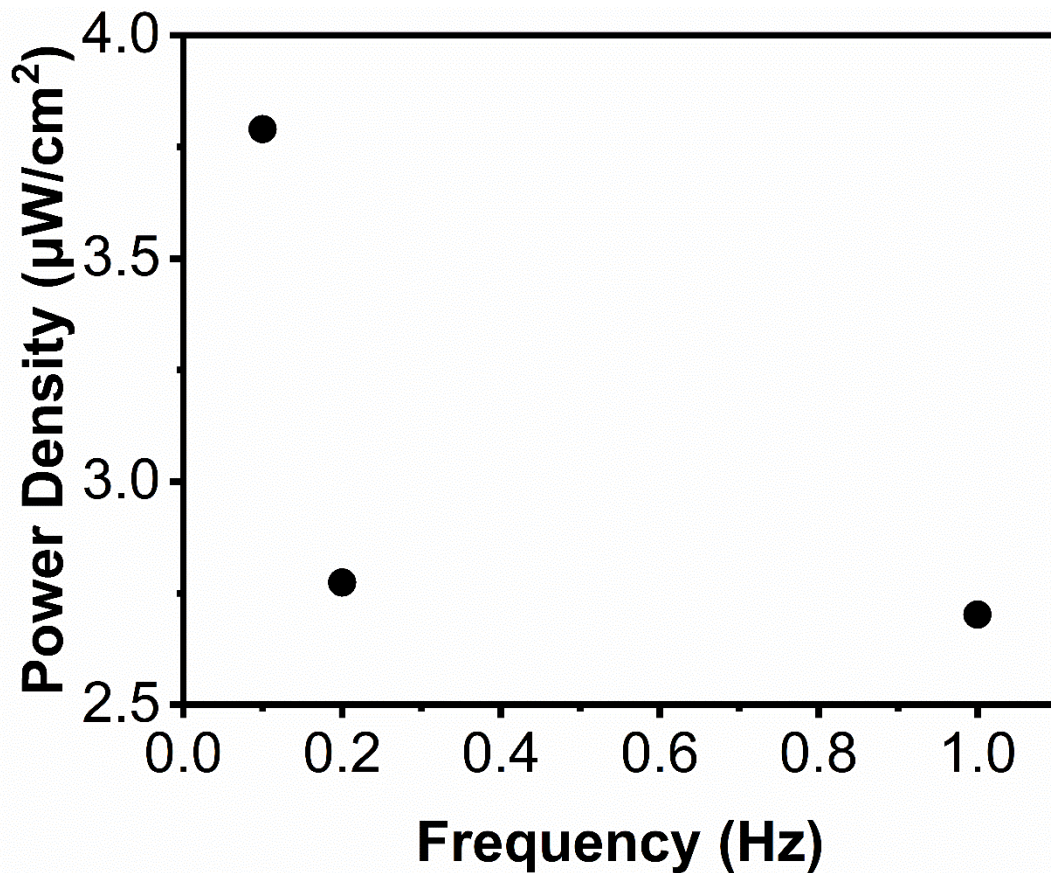
Figure 11: Power density generated during 8 mm bending tests of the PB ECG in 1M KCl for a range of bending frequencies.
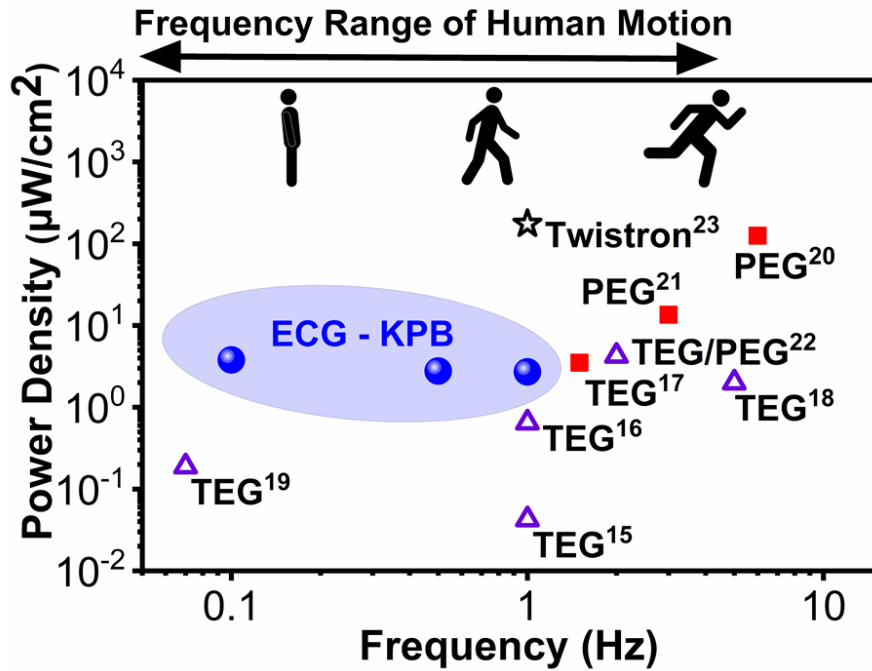
Figure 12: Power density comparison of wearable harvesters within the frequency range of human motion. Other devices include piezoelectric generators (PEG), triboelectric generators (TEG), and Twistron harvesters.

Whereas the benefit of continuous operation is not easily addressed in **Figure 12**, we emphasize the benefit of continuous operation that comes from slow ion diffusion kinetics. For example, the timescale for a potassium ion to diffuse across the 1000 nm thick electrode film and relax the stress from bending involves a diffusion coefficient of 10^{-10} cm^2/s, and hence a diffusion time of ~50 s. This diffusion or response time is in correlation with the full width at half maximum (FWHM) in our studies where continuous response was measured within 10 seconds without loss of signal.
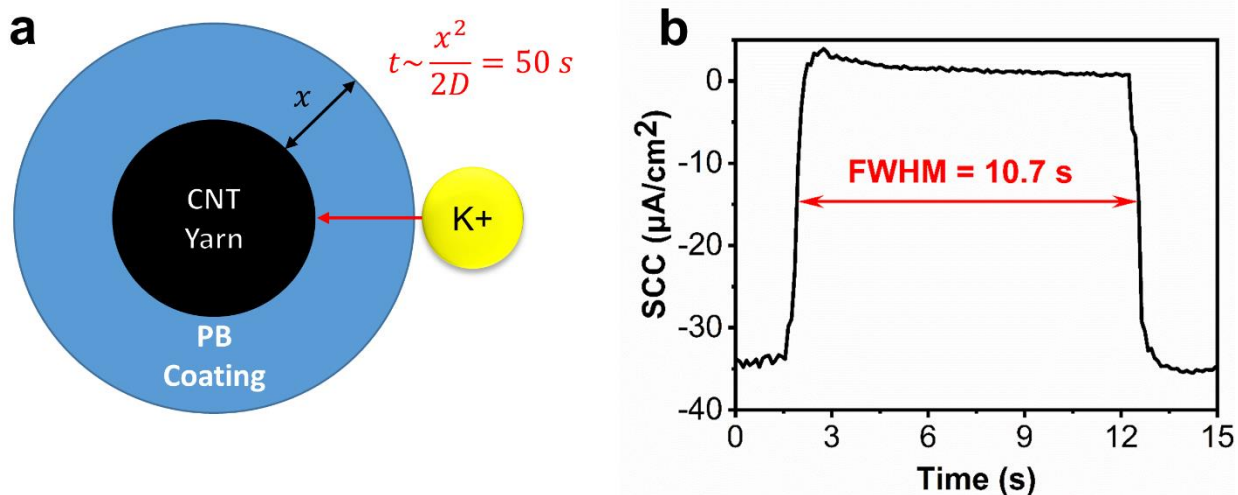
Figure 13: ECG response time analysis demonstrating diffusion-controlled timescales. (a) Characteristic diffusion time for a 1000 nm thick PB coating with a diffusion coefficient, D, of 10^{-10} cm^2/s. (b) Full width at half maximum (FWHM) of the ECG during a 10 second bend.

As decay of the signal due to diffusional relaxation of stress exceeds the time of the bending motion, a continuous current is produced through the range of extremely low frequency motions. This is an important distinction for our devices compared to the millisecond peak widths of triboelectric and piezoelectric generators since the ability to measure responses to motion over time intervals longer than the motion itself (*e.g.* continuous response) facilitates the capability to exploit this in a range of applications that extend beyond energy harvesting. One application is in the design of smart textiles that can effectively sense and identify a range of subsequent motions, allowing for tremendous opportunity in the area of health monitoring clothing and real-time motion diagnostics. A key aspect to the practical utilization of such devices is their long-term stability under environmental operation conditions due to these fibers being integrated into flexible fabric-based infrastructure systems, such as clothing, upholstery, *etc*. Therefore, we characterized long-term stability of these ECG devices up to two weeks (**Figure 14**) where we observe consistent response of the harvester over the period studied with increasing current response over time. Whereas the stability and degradation of polymer electrolytes in batteries remains an ongoing area

of research, this is commonly attributed to parasitic side reactions during charging or maintaining high voltage over long periods of time. In our ECG device, the typical voltage response is at the scale of tens of mV where such parasitic effects should not occur, and our harvester remains in an equipotential state at 0 V during rest periods until motion or bending occurs. Therefore, we expect that traditional barriers to stability for battery systems are often no longer barriers in the design and implementation of ECG devices. Further, given the capability to design these fiber devices from biocompatible materials and to form fibers that can be seamlessly integrated into a wide range of fabrics, our devices balance the performance, functionality, and integration capability that overcomes many of the barriers to other approaches reported thus far.

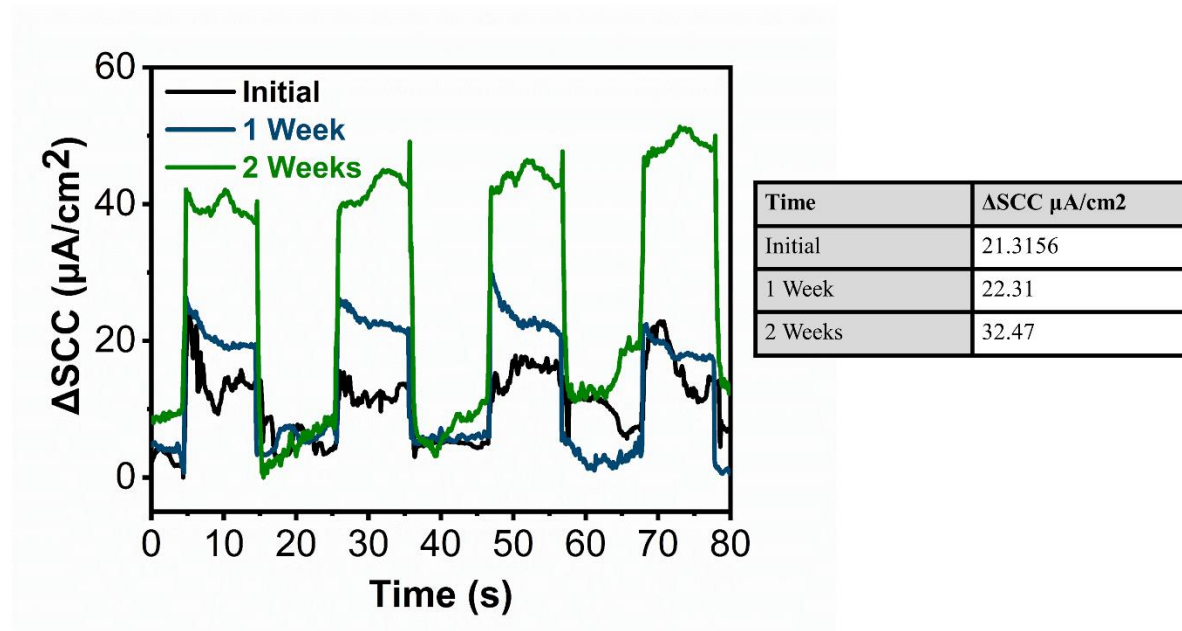| Time	ΔSCC μA/cm2
Initial	21.3156
1 Week	22.31
2 Weeks	32.47

Figure 14: SCC measurements of the PB ECG fabric with the 1M KCl/PVA solid electrolyte at an 8 mm bending radius conducted on the day of fabrication, as well as subsequently after 1 week and 2-week time intervals.

CHAPTER 4

CONCLUSIONS

In summary, we demonstrate a set of results that span from the rational mechanistic design of a fiber-based energy harvester to its application in textiles to provide continuous motion sensing and energy harvesting capability. Using biocompatible Prussian blue active materials which facilitate Li, Na, or K insertion, our work demonstrates evidence that K-ion insertion is best suited for optimal power and energy output in an ECG, which is in contrast to the suitability of similar materials in a battery. Further, we show a PB ECG fiber-based device with peak power output of 3.8 μW/cm^2 during bending at 0.1 Hz frequency with a 4 mm bending radius, which is in a frequency range relevant to human motion and with peak power competitive with TEG or PEG approaches that are design-limited either by response time or integration capability. Further, we demonstrate the capability to produce solid-state fibers that can be sewn into clothing and textiles which can provide continuous response of human motion, including bending of an arm or bending of a finger. Unlike other approaches for energy harvesting that result in either a configuration challenging to scale to wearables or a high frequency fast pulse of power generation that is poorly suited to low-frequency human motion, we show this approach with fiber-based ECGs to command high performance, continuous operation, and straightforward scaling to textiles and fiber-based form factors. In a future where wearables will enable greater insight into human health, human activity, and provide platforms for entertainment and productivity – these ECG devices can play a role as either a sensing media for motion and human health as well as a power source that converts human motion into usable or storable energy.

APPENDIX

Extrapolating Motion Sensing Range

Experimental ECG bending tests demonstrate that a stable signal can be obtained and that the signal scales with bending radius through an inverse relationship down to a 4 mm bending radius. On the upper end of bending radii, the ECG current response at bending radii larger than the 14.25 mm test can be extrapolated from the data using the empirical relationship of the voltage scaling with the inverse of the bending angle, as $\Delta E = 233\frac{1}{R} - 6.79$. The standard deviation of the OCV from a 1-hour test while the ECG is flat gives a value of 0.00213 V. This means at a bending radius of ~33 mm, the signal is indistinguishable from the noise of the OCV measurement.

REFERENCES

1. Zhou, M., Al-Furjan, M. S. H., Zou, J. & Liu, W. A review on heat and mechanical energy harvesting from human – Principles, prototypes and perspectives. *Renew. Sustain. Energy Rev.* **82**, 3582–3609 (2018).

2. Rabaey, J. M., Ammer, M. J., Silva, J. L. da, Patel, D. & Roundy, S. PicoRadio supports ad hoc ultra-low power wireless networking. *Computer (Long. Beach. Calif).* **33**, 42–48 (2000).

3. Yeatman, E. M. Advances in power sources for wireless sensor nodes. in *Proceedings of International Workshop on Wearable and Implantable Body Sensor Networks* (2004).

4. Holmes, A. S., Guodong, H., Pullen, K. R. & Buffard, K. R. *Axial-flow microturbine with electromagnetic generator: design, CFD simulation, and prototype demonstration*. (2004). doi:10.1109/MEMS.2004.1290648

5. Yaglioglu, O. Modeling and Design Considerations for a Micro-hydraulic Piezoelectric Power Generator. (MIT, 2002).

6. Ramsay, M. & Clark, W. Piezoelectric energy harvesting for bio-MEMS applications. *Proceeding Smart Struct. Mater.* **4332**, 429–438 (2001).

7. Tan, Y. & Panda, S. Review of Energy Harvesting Technologies for Sustainable Wireless Sensor Network 15 0 Review of Energy Harvesting Technologies for Sustainable Wireless Sensor Network. (2010).

8. Yildiz, F. Potential Ambient Energy-Harvesting Sources and Techniques. *J. Technol. Stud.* **35**, 40–48 (2009).

9. Lai, Y.-C. *et al.* Single-Thread-Based Wearable and Highly Stretchable Triboelectric Nanogenerators and Their Applications in Cloth-Based Self-Powered Human-Interactive and Biomedical Sensing. *Adv. Funct. Mater.* **27**, 1604462 (2017).

10. Yang, Y. *et al.* Coaxial Triboelectric Nanogenerator and Supercapacitor Fiber-Based Self-Charging Power Fabric. *ACS Appl. Mater. Interfaces* **10**, 42356–42362 (2018).

11. Pu, X. *et al.* Ultrastretchable, transparent triboelectric nanogenerator as electronic skin for biomechanical energy harvesting and tactile sensing. *Sci. Adv.* **3**, e1700015–e1700015 (2017).

12. Pu, X. *et al.* Wearable Self-Charging Power Textile Based on Flexible Yarn Supercapacitors and Fabric Nanogenerators. *Adv. Mater.* **28**, 98–105 (2016).

13. Dhakar, L., Pitchappa, P., Tay, F. E. H. & Lee, C. An intelligent skin based self-powered finger motion sensor integrated with triboelectric nanogenerator. *Nano Energy* **19**, 532–540 (2016).

14. Maharjan, P., Toyabur, R. M. & Park, J. Y. A human locomotion inspired hybrid nanogenerator for wrist-wearable electronic device and sensor applications. *Nano Energy*

46, 383–395 (2018).

15. Liu, H. *et al.* A non-resonant rotational electromagnetic energy harvester for low-frequency and irregular human motion. *Appl. Phys. Lett.* **113**, 203901 (2018).

16. Fan, K., Cai, M., Liu, H. & Zhang, Y. Capturing energy from ultra-low frequency vibrations and human motion through a monostable electromagnetic energy harvester. *Energy* **169**, 356–368 (2019).

17. Song, S. & Yun, K. S. Design and characterization of scalable woven piezoelectric energy harvester for wearable applications. *Smart Mater. Struct.* **24**, 45008 (2015).

18. Siddiqui, S. *et al.* High-performance flexible lead-free nanocomposite piezoelectric nanogenerator for biomechanical energy harvesting and storage. *Nano Energy* **15**, 177–185 (2015).

19. Li, X. *et al.* 3D Fiber-Based Hybrid Nanogenerator for Energy Harvesting and as a Self-Powered Pressure Sensor. *ACS Nano* **8**, 10674–10681 (2014).

20. Kim, S. H. *et al.* Harvesting electrical energy from carbon nanotube yarn twist. *Science (80-.).* **357**, 773 LP – 778 (2017).

21. Muralidharan, N., Li, M., Carter, R. E., Galioto, N. & Pint, C. L. Ultralow Frequency Electrochemical–Mechanical Strain Energy Harvester Using 2D Black Phosphorus Nanosheets. *ACS Energy Lett.* **2**, 1797–1803 (2017).

22. Muralidharan, N., Afolabi, J., Share, K., Li, M. & Pint, C. L. A Fully Transient Mechanical Energy Harvester. *Adv. Mater. Technol.* **3**, 1800083 (2018).

23. Cannarella, J. & Arnold, C. B. Toward Low-Frequency Mechanical Energy Harvesting Using Energy-Dense Piezoelectrochemical Materials. *Adv. Mater.* **27**, 7440–7444 (2015).

24. Kim, S. *et al.* Electrochemically driven mechanical energy harvesting. *Nat. Commun.* **7**, 10146 (2016).

25. Larché, F. C. & Cahn, J. W. Overview no. 41 The interactions of composition and stress in crystalline solids. *Acta Metall.* **33**, 331–357 (1985).

26. Jana, A., Woo, S. I., Vikrant, K. S. N. & García, R. E. Electrochemomechanics of lithium dendrite growth. *Energy Environ. Sci.* **12**, 3595–3607 (2019).

27. Vikrant, K. S. N., Chueh, W. C. & García, R. E. Charged interfaces: electrochemical and mechanical effects. *Energy Environ. Sci.* **11**, 1993–2000 (2018).

28. Bucci, G. (1) *et al.* The effect of stress on battery-electrode capacity. *J. Electrochem. Soc.* **164**, A645–A654 (2017).

29. Yang, H., Liang, W., Wang, C. & Zhang, S. Strong kinetics-stress coupling in lithiation of Si and Ge anodes. *Extrem. Mech. Lett.* **2**, 1–6 (2015).

30. Koerver, R. *et al.* Chemo-mechanical expansion of lithium electrode materials – on the route to mechanically optimized all-solid-state batteries. *Energy Environ. Sci.* **11**, 2142–2158 (2018).

31. Muralidharan, N., Carter, R., Oakes, L., Cohn, A. P. & Pint, C. L. Strain Engineering to Modify the Electrochemistry of Energy Storage Electrodes. *Sci. Rep.* **6**, 27542 (2016).

32. Muralidharan, N. *et al.* Tunable Mechanochemistry of Lithium Battery Electrodes. *ACS Nano* **11**, 6243–6251 (2017).

33. Oakes, L. *et al.* Interface strain in vertically stacked two-dimensional heterostructured carbon-MoS2 nanosheets controls electrochemical reactivity. *Nat. Commun.* **7**, 11796 (2016).

34. Ricci, F. & Palleschi, G. Sensor and biosensor preparation, optimisation and applications of Prussian Blue modified electrodes. *Biosens. Bioelectron.* **21**, 389–407 (2005).

35. Bariya, M., Nyein, H. Y. Y. & Javey, A. Wearable sweat sensors. *Nat. Electron.* **1**, 160–171 (2018).

36. Bariya, M. *et al.* Roll-to-Roll Gravure Printed Electrochemical Sensors for Wearable and Medical Devices. *ACS Nano* **12**, 6978–6987 (2018).

37. Wang, C. *et al.* Advanced Carbon for Flexible and Wearable Electronics. *Adv. Mater.* **31**, 1801072 (2019).

38. Guo, J. *et al.* Highly Stretchable, Strain Sensing Hydrogel Optical Fibers. *Adv. Mater.* **28**, 10244–10249 (2016).

39. Lee, S. *et al.* Ag Nanowire Reinforced Highly Stretchable Conductive Fibers for Wearable Electronics. *Adv. Funct. Mater.* **25**, 3114–3121 (2015).

40. Heikenfeld, J. *et al.* Wearable sensors: modalities{,} challenges{,} and prospects. *Lab Chip* **18**, 217–248 (2018).

41. Gao, W. *et al.* Fully integrated wearable sensor arrays for multiplexed in situ perspiration analysis. *Nature* **529**, 509 (2016).

42. Gualandi, I. *et al.* Textile Organic Electrochemical Transistors as a Platform for Wearable Biosensors. *Sci. Rep.* **6**, 33637 (2016).

43. Kim, J., Campbell, A. S., de Ávila, B. E.-F. & Wang, J. Wearable biosensors for healthcare monitoring. *Nat. Biotechnol.* **37**, 389–406 (2019).

44. Muralidharan, N. *et al.* Carbon Nanotube Reinforced Structural Composite Supercapacitor. *Sci. Rep.* **8**, 17662 (2018).

45. Meng, C. *et al.* Multifunctional Structural Ultrabattery Composite. *Nano Lett.* **18**, 7761–7768 (2018).

46. Moyer, K. *et al.* Carbon fiber reinforced structural lithium-ion battery composite: Multifunctional power integration for CubeSats. *Energy Storage Mater.* **24**, 676–681 (2020).

47. Moyer, K., Boucherbil, N. A., Zohair, M., Eaves-Rathert, J. & Pint, C. L. Polymer reinforced carbon fiber interfaces for high energy density structural lithium-ion batteries. *Sustain. Energy Fuels* (2020). doi:10.1039/D0SE00263A

48. Westover, A. S. *et al.* Multifunctional high strength and high energy epoxy composite structural supercapacitors with wet-dry operational stability. *J. Mater. Chem. A* **3**, 20097–20102 (2015).

49. Huang, Y. *et al.* From Industrially Weavable and Knittable Highly Conductive Yarns to Large Wearable Energy Storage Textiles. *ACS Nano* **9**, 4766–4775 (2015).

50. Wang, G. *et al.* Wearable supercapacitors on polyethylene terephthalate fabrics with good wash fastness and high flexibility. *J. Power Sources* **367**, 34–41 (2017).

51. Huang, Q., Wang, D. & Zheng, Z. Textile-Based Electrochemical Energy Storage Devices. *Adv. Energy Mater.* **6**, 1600783 (2016).

52. Huang, Y. *et al.* Weavable, Conductive Yarn-Based NiCo//Zn Textile Battery with High Energy Density and Rate Capability. *ACS Nano* **11**, 8953–8961 (2017).

53. Jost, K. *et al.* Natural Fiber Welded Electrode Yarns for Knittable Textile Supercapacitors. *Adv. Energy Mater.* **5**, 1401286 (2015).

54. Itaya, K., Ataka, T. & Toshima, S. Spectroelectrochemistry and electrochemical preparation method of Prussian blue modified electrodes. *J. Am. Chem. Soc.* **104**, 4767–4772 (1982).

55. Moyer, K. *et al.* High-rate potassium ion and sodium ion batteries by co-intercalation anodes and open framework cathodes. *Nanoscale* **10**, 13335–13342 (2018).

56. Assis, L. M. N., Leones, R., Kanicki, J., Pawlicka, A. & Silva, M. M. Prussian blue for electrochromic devices. *J. Electroanal. Chem.* **777**, 33–39 (2016).

57. Du, D., Wang, M., Qin, Y. & Lin, Y. One-step electrochemical deposition of Prussian Blue–multiwalled carbon nanotube nanocomposite thin-film: preparation{,} characterization and evaluation for H2O2 sensing. *J. Mater. Chem.* **20**, 1532–1537 (2010).

58. Mažeikienė, R., Niaura, G. & Malinauskas, A. Electrocatalytic reduction of hydrogen peroxide at Prussian blue modified electrode: An in situ Raman spectroelectrochemical study. *J. Electroanal. Chem.* **660**, 140–146 (2011).

59. Wu, X., Leonard, D. P. & Ji, X. Emerging Non-Aqueous Potassium-Ion Batteries: Challenges and Opportunities. *Chem. Mater.* **29**, 5031–5042 (2017).

60. Pramudita, J. C. *et al.* Sodium uptake in cell construction and subsequent in operando electrode behaviour of Prussian blue analogues, Fe[Fe(CN)6]1-x·yH2O and FeCo(CN)6. *Phys. Chem. Chem. Phys.* (2014). doi:10.1039/c4cp02676d

61. Wang, B. *et al.* Gradient substitution: An intrinsic strategy towards high performance sodium storage in Prussian blue-based cathodes. *J. Mater. Chem. A* (2018). doi:10.1039/c8ta02291g

62. Takachi, M., Matsuda, T. & Moritomo, Y. Redox reactions in prussian blue analogue films with fast Na+ intercalation. *Jpn. J. Appl. Phys.* (2013). doi:10.7567/JJAP.52.090202

63. Nozaki, S. *et al.* Radius of curvature at the talocrural joint surface: inference of subject-specific kinematics. *Surg. Radiol. Anat.* **41**, 53–64 (2019).

64. Kosel, J., Giouroudi, I., Scheffer, C., Dillon, E. & Erasmus, P. Anatomical Study of the Radius and Center of Curvature of the Distal Femoral Condyle. *J. Biomech. Eng.* **132**, (2010).

65. Zhong, J. *et al.* Stretchable Self-Powered Fiber-Based Strain Sensor. *Adv. Funct. Mater.* **25**, 1798–1803 (2015).

66. Félix, G. *et al.* Elasticity of Prussian-Blue-Analogue Nanoparticles. *Eur. J. Inorg. Chem.* (2018). doi:10.1002/ejic.201700796